The final publication is available at

https://doi.org/10.1016/j.ceramint.2022.01.339

Additional Information

Influence of $Zn(NO_3)_2$ concentration during the ZnO electrodeposition on TiO_2 nanosponges used in photoelectrochemical applications

P.J. Navarro-Gázquez[1], E. Blasco-Tamarit[1], M.J. Muñoz-Portero[1], B. Solsona[2], R.M. Fernández-Domene[2], R. Sánchez-Tovar[2], J. García-Antón[1,*]

[1]*Instituto Universitario de Seguridad Industrial, Radiofísica y Medioambiental (ISIRYM). Universitat Politècnica de València. Camino de Vera s/n, 46022 Valencia, Spain.*

[2]*Departamento de Ingeniería Química, Universitat de València, Av. de las Universitats, s/n, 46100 Burjassot, Spain.*

Tel. 34-96-387 76 32, e-mail: jgarciaa@iqn.upv.es

Abstract

TiO_2/ZnO hybrid nanostructures were formed by electrochemical anodization of titanium and subsequently ZnO electrodeposition. Different $Zn(NO_3)_2$ concentrations were used for electrodeposition (10 to 60 mM). A structural, morphological, and compositional characterisation was performed using FE-SEM, TEM, AFM, XRD, UV-Visible spectroscopy, and band gap measurements. It was reported that the morphology of the nanostructures changed with the $Zn(NO_3)_2$ concentration. Nanosponges were observed for concentrations from 10 mM to 30 mM whereas at 40 mM the morphology changed to well-defined ZnO hexagonal nanorods. At 50 mM a surface covered by ZnO with undefined rods could be seen and, at 60 mM, a morphology of nanoplatelets was observed. Besides, as $Zn(NO_3)_2$ concentration increased, the ZnO amount, the roughness, and the ZnO crystalline size also increased, while the band gap decreased. Electrochemical characterisation of nanostructures was performed by water splitting,

1

stability to photocorrosion, EIS, and Mott-Schottky tests. The optimal samples were TiO$_2$/ZnO hybrid nanostructures electrodeposited with 30 mM Zn(NO$_3$)$_2$, since they were stable against photocorrosion and, compared to TiO$_2$ nanosponges, showed an increase in photoelectrochemical activity of 204 %, a lower resistance to charge transfer, and a higher donor density. Overall, the most efficient samples presented an intermediate Zn-loading because of a maximization of the TiO$_2$-ZnO interaction and the prevention of the formation of non-interacting ZnO structures.

Keywords: TiO$_2$/ZnO hybrid nanostructures, titanium dioxide, zinc oxide, Zn(NO$_3$)$_2$ concentration, photoelectrochemical water splitting.

2

1. Introduction

The use of photocalysts for energetic and environmental applications such as the photoelectrochemical production of hydrogen [1–3] or the organic pollutant degradation [4–6] is having an increasing impact. One of the main requirements of photocatalysts is having an adequate band gap so that electrons from the valence band can be transferred to the conduction band when they are irradiated with light of a specific wavelength. Thus, electron-hole pairs are generated to produce the reduction/oxidation of compounds.

One of the most studied semiconductors used as a photocatalyst is titanium dioxide (TiO_2) [2,5,7–13]. TiO_2 offers good performance for photoelectrochemical applications because it has high electron carrier movement, chemical stability, non-toxicity, relative low cost, and high photocatalytic activity [14]. Increasing the surface area of TiO_2 is crucial in order to obtain high efficiencies. For this reason, a great variety of morphologies has been developed over the last years such as nanotubes, nanowires, nanoflowers, nanorods, nanosheets or nanobelts [15]. Usually, TiO_2 nanostructures are synthesised based on hydrothermal methods, sol-gel methods, chemical vapour deposition, electrodeposition, and electrochemical anodization [8]. Of all of these, electrochemical anodization makes it possible to synthesise different nanostructures directly on a metallic substrate, so it is not necessary to carry out a subsequent stage of compaction or synthesis on a conductive substrate. In addition, it has the advantage that it is not necessary to use high temperatures or pressures since it is usually carried out at room temperature and atmospheric pressure [7,10,13]. For example, a new type of TiO_2 nanostructure (nanosponge) was recently developed by performing an electrochemical anodization under hydrodynamic conditions in an electrolyte composed of glycerol, water, and ammonium fluoride (NH_4F). TiO_2 nanosponges form a strongly interconnected network with directly connected electron paths and a high specific area [10,16–18].

3

The main drawback of using TiO_2 as a photocatalyst is its wide band gap value (~ 3.2 eV for TiO_2 anatase phase, λ = 390 nm) which limits its photoelectrochemical applications to ultraviolet irradiation range [19]. The band gap of a photocatalyst determines its absorption range within the solar spectrum. Electrons are excited from the valence band to the conduction band when a semiconductor absorbs photons with equal or greater energy than its band gap, generating electron-hole pairs. These two species (electron-hole) can recombine or participate in redox reactions. The value of the band gap (E_g) is inversely proportional to the wavelength of the radiation photons (λ), according to Eq. 1.

$$E_g = \frac{h \cdot c}{\lambda}$$

Eq. 1

Where h is the Planck's constant ($6.626 \cdot 10^{-34}$ J·s^{-1}) and c is the speed of light in vacuum (3.10^8 m·s^{-1}).

Decreasing the band gap allows the extension of the photo-response of the semiconductors towards wavelengths of the visible range (less energetic than the ultraviolet irradiation range but which constitutes the largest part of the solar spectrum). This fact results in an increase in the photogeneration of electron-hole pairs, improving the photoelectrochemical performance of the photocatalysts in any photoelectrochemical application.

In order to overcome this inconvenience, different elements such as noble metals [20,21] or ions [16,17,22] have been often added to TiO_2 nanostructures. However, in recent years, the formation of hybrid nanostructures is attracting more interest [23,24]. Thus, hybrid nanostructures composed of TiO_2 and zinc oxide (ZnO) have been used in this research.

4

The synthesis of TiO$_2$/ZnO hybrid nanostructures has the advantage that both semiconductors have a similar band gap (3.2 eV for TiO$_2$ anatase phase and 3.3 eV for ZnO) [25–27]. Therefore, electrons and holes of the conduction and valence bands of TiO$_2$ and ZnO can be combined, reducing the recombination processes by irradiating the nanostructures with light. Furthermore, as ZnO has a more negative conduction band (-0.32 V vs SHE [28]) than TiO$_2$ (-0.27 V vs SHE [29]), combining both semiconductors improves the photocatalytic activity of nanostructures for photoelectrochemical applications [25,27,30–33].

Hybrid nanostructures can be formed from a variety of methods such as atomic layer deposition [34], the hydrothermal method [35,36], or the sol-gel method [37,38]. However, in this work, the process of ZnO electrodeposition on TiO$_2$ nanosponges has been used because it allows the incorporation of ZnO into TiO$_2$ nanostructures at moderate temperatures, at atmospheric pressure, and in short times. In addition, it makes it possible to control the amount of electrodeposited ZnO and the morphology of the nanostructures [39–42].

2. Experimental procedure

2.1. *Synthesis of TiO$_2$/ZnO hybrid photocatalysts*

In this work, the formation of TiO$_2$/ZnO hybrid nanostructures was carried out by ZnO electrodeposition on crystalline TiO$_2$ nanosponges, following the method developed by authors in a previous work [43]. First, TiO$_2$ nanosponges were synthesised by electrochemical anodization of titanium (Ti) under hydrodynamic conditions at room temperature [10,16,17]. For this purpose, metallic titanium rod (99.3 % purity and 8 mm in diameter) was polished with 240-4000 silicon carbide (SiC) papers to obtain a mirror

surface. After that, the sample was sonicated in ethanol for 2 minutes, rinsed with distilled

water, and dried with air. Finally, the sample was covered with a polytetrafluoroethylene

(PTFE) coating (0.5 cm^2 area exposed to the electrolyte). Polished Ti was used as working

electrode, and a platinum foil as counter electrode. A solution composed of glycerol/water

(60/40 vol.%) with 0.27 M NH_4F at room temperature was used as electrolyte. The

potential was increased from 0 to 30 V at a constant rate of 0.1 V/s applying subsequently

30 V for 3 hours. TiO_2 nanosponges were then annealed at 450 ºC for 1 hour to obtain the

anatase crystalline structure of TiO_2. Finally, the ZnO electrodeposition was carried out

at a potential of -0.86 $V_{Ag/AgCl}$ for 15 minutes at 75 ºC with zinc nitrate hexahydrate

($Zn(NO_3)_2 \cdot 6H_2O$) concentrations between 10 and 60 mM. TiO_2 nanosponges were used

as working electrodes, a platinum tip was used as counter electrode, and an Ag/AgCl (3

M KCl) electrode was used as reference electrode.

2.2. *Structural, compositional, and morphological characterisation of photocatalysts*

The structural, compositional, and morphological characterisation of the nanostructures

was carried out. Field Emission Scanning Electron Microscopy (FE-SEM) with Energy-

Dispersive X-Ray Spectroscopy (EDX), Transmission Electron Microscopy (TEM), and

high-resolution TEM (HRTEM) were used to evaluate the morphology and the chemical

composition of photocatalysts. FE-SEM measurements were performed in a Zeiss Ultra

55 microscope working at 2 kV with EDX working at 20 kV. TEM measurements were

performed using a FEI Field Emission Gun (FEG) TECNAI G2 F20 S-TWIN microscope

working at 200 kV with EDX in TEM nanoprobe mode. For TEM experiments, a piece

of the samples was cut and deposited onto a holey carbon film supported on a copper grid.

In addition, the roughness of the nanostructures was characterised using an Atomic Force

Microscope (AFM) WITec alpha300A, by the calculation of the Sa parameter

6

(arithmetical mean height of the surface), and the Sq parameter (root mean square). The AC mode (an intermittent contact regimen) was used with an oscillating cantilever (0.5 V).

X-Ray Diffraction (XRD) was used to verify the ZnO formation, to identify the composition of the phases of the crystals, and to obtain the crystallite size of the nanostructures. In order to carry out this process, a Bruker D8AVANCE diffractometer with Cu radiation operating at 30 mA and 40 Kv was used.

Finally, UV-Visible spectroscopy measurements of the samples were carried out within the 200-850 nm range using a Shimadzu spectrometer. The value of the band gap, E_g, was obtained by extrapolating the linear fitted region at $[F(R(\infty))\ h\upsilon]^2 = 0$ in the plot of $[F(R(\infty))\ h\upsilon]^2$ versus $h\upsilon$.

2.3. Electrochemical characterisation of the photocatalysts

The electrochemical characterisation was carried out in both dark and illuminated (AM 1.5, 100 mW·cm^{-2}) conditions in a cell composed of three electrodes connected to a potentiostat (Autolab PGSTAT302N) where the nanostructures were the working electrodes, a platinum tip was the counter electrode, and an Ag/AgCl (3 M KCl) electrode was the reference electrode. A 0.1 M NaOH aqueous solution was used as electrolyte.

The photoelectrochemical response of nanostructures was measured by water splitting tests performed between -1 and 0.84 $V_{Ag/AgCl}$ with a scan rate of 2 mV·s^{-1} by chopped light irradiation. In addition, stability tests to photocorrosion were also carried out applying a potential of 0.84 $V_{Ag/AgCl}$ for 1 hour. Electrochemical Impedance Spectroscopy (EIS) and Mott-Schottky tests were performed to analyse the electrochemical behaviour of the nanostructures that presented the best photoelectrocatalytic performance. On the

7

one hand, EIS was carried out at 0.6 $V_{Ag/AgCl}$ in a frequency range from 100 kHz to 10 mHz with a 10 mV signal amplitude. On the other hand, Mott-Schottky tests were performed from 0.8 to -0.9 $V_{Ag/AgCl}$ at a frequency of 10 kHz with an amplitude signal of 10 mV.

3. Results and discussion

3.1. Synthesis of TiO$_2$/ZnO hybrid photocatalysts

The formation of TiO$_2$/ZnO hybrid nanostructures was performed in two phases, following the method optimized by authors in a previous work [43]. First, the synthesis of TiO$_2$ nanosponges with crystalline structure was carried out, and later, the ZnO electrodeposition was performed. Fig. S1a shows the current density vs time obtained during the anodization process of TiO$_2$ nanosponges, while Fig. S1b shows the current density vs time obtained during the ZnO electrodeposition process.

The synthesis of TiO$_2$ nanosponges took place in three stages (Fig. S1a). In the first stage, a TiO$_2$ compact layer was formed on the Ti metallic substrate and, consequently, the resistance to charge transfer increased, thus decreasing the current density. Then, in the second stage, fluorides of the solution began dissolving the TiO$_2$ compact layer, thus reducing the resistance to charge transfer. This attack produced the formation of small nanopores along the entire surface of TiO$_2$. Subsequently, the current density decreased again as a consequence of the beginning of the formation of a nanostructured and irregular layer. Finally, in the third stage, the formation and growth of a nanostructured layer (nanosponge) occurred until reaching a state of equilibrium between the formation of oxide at the metal/oxide interface and the dissolution of oxide at the oxide/electrolyte interface.

8

Once the synthesis of TiO$_2$ nanosponges was finished, a heat treatment was carried out to transform the amorphous TiO$_2$ to the anatase phase. After that, the ZnO electrodeposition process took place. The mechanism of ZnO formation from Zn(NO$_3$)$_2$ has been studied and reported [39–42]. During the ZnO electrodeposition process, ZnO was formed by the dehydration reaction of the complex Zn(OH)$_2$ generated from the union of OH$^-$ and Zn^{+2} ions. OH$^-$ ions were formed on the TiO$_2$ surface as a consequence of the nitrate reduction reactions. In Fig. S1b, it is observed that the current density increases as the Zn(NO$_3$)$_2$ concentration increases. The increase in the current density is associated with a greater conductivity of the solution caused by a higher quantity of OH$^-$ and Zn^{+2} ions present in the solution. For this reason, the rise in current density is related with a higher ZnO formation [42]. Fig. S1b shows that in the initial moments there is a sudden drop in current density that is related to the nucleation of ZnO crystals on the TiO$_2$ surface. Subsequently, the current density undergoes an increase/stabilization stage, which is associated with the shape and growth of the ZnO crystals. The growth of ZnO crystals is controlled by the diffusion of Zn^{+2} and the generation of OH$^-$. If the diffusion of Zn^{+2} is slower than the generation of OH$^-$ ions, the ZnO growth takes place in the longitudinal axis, but if the diffusion of Zn^{+2} is faster than the generation of OH$^-$ ions, transversal growth predominates over longitudinal growth. The higher current density obtained by increasing the Zn(NO$_3$)$_2$ concentration is associated to different rates of generation of OH$^-$ and diffusion of Zn^{+2}, which causes different growth rates of ZnO crystals, both in the longitudinal and the transverse axis. As it will be shown in section 3.2.1., the transversal growth rate of ZnO crystals is more remarkable as the current density increases during the electrodeposition process. Therefore, the growth rate and orientation of the ZnO crystals change as the Zn(NO$_3$)$_2$ concentration increases, which can lead to the formation of different structures [44].

9

3.2. Structural, compositional, and morphological characterisation

Once the synthesis of photocatalysts was finished, a structural, compositional, and morphological characterisation was performed. This study was carried out using FE-SEM with EDX, TEM, AFM, UV-Visible spectroscopy, and band gap measurements.

3.2.1. Field Emission Scanning Electron Microscopy with Energy-Dispersive X-Ray Spectroscopy

Firstly, the influence of $Zn(NO_3)_2$ concentration on the morphological characteristics of TiO_2/ZnO hybrid nanostructures was analysed by FE-SEM with EDX. Fig. 1 shows representative images at two different magnifications of TiO_2/ZnO hybrid nanostructures electrodeposited with $Zn(NO_3)_2$ concentrations between 10 and 60 mM.

Fig 1 shows a nanosponge-shaped structure in samples electrodeposited with $Zn(NO_3)_2$ concentrations between 10 and 30 mM. Besides, the formation of ZnO crystals on the TiO_2 nanosponge can be observed as $Zn(NO_3)_2$ concentration increases from 10 to 30 mM. However, when $Zn(NO_3)_2$ concentrations between 40 and 60 mM were used, different morphologies were observed. In the first place, thanks to the dendritic growth of ZnO crystals on the TiO_2 nanosponges, a well-defined and uniform morphology composed of ZnO hexagonal nanorods oriented transversely to the TiO_2 surface can be seen in Fig. 1d. The height of ZnO nanorods was between 120 and 190 nm, while the diameters obtained were between 17 and 19 nm. In the second place, Fig. 1e shows that, by increasing the $Zn(NO_3)_2$ concentration to 50 mM, crystal growth occurs both transversely and longitudinally, which hinders the dendritic growth of ZnO crystals and, therefore, the formation of well-defined ZnO nanorods. Finally, with a $Zn(NO_3)_2$ concentration of 60 mM (Fig. 1f), a dense nanoplatelet morphology appears widely

distributed over the entire surface. This type of morphology is generated by the deposition of ZnO crystals on the TiO_2 surface. It must be noted that, in some regions, these nanoplatelets stick out from the surface of the sample.

ZnO nanostructures grew mainly in the vertical axis when $Zn(NO_3)_2$ concentrations between 10 mM and 40 mM were used during the electrodeposition process. However, the ZnO layer was extended uniformly along the entire horizontal axis when $Zn(NO_3)_2$ concentrations of 50 and 60 mM were used. The transverse growth was more remarkable as the current density during the electrodeposition process increased. The longitudinal growth of the nanostructures predominated for $Zn(NO_3)_2$ concentrations between 10 mM and 40 mM, while the transverse growth was similar or higher than the longitudinal growth for $Zn(NO_3)_2$ concentrations of 50 mM and 60 mM.

Additionally, Fig. S2 shows representative images of cross sections of the TiO_2 nanosponges and the TiO_2/ZnO hybrid nanostructures electrodeposited with $Zn(NO_3)_2$ concentrations of 10, 30, and 60 mM. The samples had a thickness of 3 ± 0.8 μm regardless of the ZnO amount. The cross section of the TiO_2/ZnO hybrid nanostructures electrodeposited with a $Zn(NO_3)_2$ concentration of 60 mM (Fig. S2d) is very different from the rest due to the formation of a nanostructured layer of ZnO shaped like nanoplatelets on the TiO_2 nanosponge. Then, an EDX analysis was performed to determine the composition of the nanostructures and to verify that, by increasing the $Zn(NO_3)_2$ concentration, the amount of electrodeposited ZnO on TiO_2 nanosponges increases. Table 1 shows the composition of TiO_2 nanosponges and TiO_2/ZnO hybrid nanostructures electrodeposited with $Zn(NO_3)_2$ concentrations between 10 and 60 mM. Fig. S3 shows, as an example, the EDX spectra of TiO_2/ZnO hybrid nanostructures electrodeposited with 10, 30, 40, and 60 mM $Zn(NO_3)_2$. In this figure, it can be observed that the intensity of the peaks related to Zn increases as $Zn(NO_3)_2$ concentration increases.

11

Table 1 shows that, by increasing the $Zn(NO_3)_2$ concentration, the Zn ratio increases, while the ratio of Ti and O decreases. During the formation of TiO_2/ZnO hybrid nanostructures, the O/Ti atomic ratio considerably increased with the $Zn(NO_3)_2$ concentration, while the O/Zn atomic ratio decreased approaching to 1. Therefore, this fact indicates that Zn was added in its oxidation state II (ZnO).

So, as it was expected, the higher the $Zn(NO_3)_2$ concentration during the electrodeposition process is, the greater the ZnO amount in the nanostructures will be [33,35,39,42]. By using $Zn(NO_3)_2$ concentrations between 10 and 30 mM, the amount of Zn gradually increases. However, with concentrations between 40 and 50 mM $Zn(NO_3)_2$, the increase in the Zn ratio is more pronounced due to the formation of ZnO nanostructures that completely cover the surface of TiO_2 nanosponges, as shown in Fig. 1d to f.

In addition, EDX mappings of TiO_2 nanosponges and TiO_2/ZnO hybrid nanostructures electrodeposited with $Zn(NO_3)_2$ concentrations from 10 to 60 mM were performed (Fig. S4). These mappings show that ZnO is well distributed over the entire surface without forming agglomerations. Besides, it can be observed in Fig. S4 that, at $Zn(NO_3)_2$ concentrations higher than 30 Mm, the presence of Zn in the nanostructures is more marked.

3.2.2. Transmission Electron Microscopy

A detailed transmission electron microscopy (TEM) and high-resolution electron microscopy (HRTEM) study was undertaken to get further insights into the morphological properties of the samples. This study was carried out using a piece of the nanostructure obtained by scratching the surface of the sample holder so that the active material is drawn. Fig. S5 shows representative TEM images of TiO_2/ZnO hybrid

nanostructures electrodeposited with low (TiO$_2$/ZnO_10mM), medium (TiO$_2$/ZnO_30mM) and high (TiO$_2$/ZnO_60mM) concentrations of Zn(NO$_3$)$_2$.

It can be observed that the morphology of these nanostructures highly depends on the composition. In the sample prepared with the lowest Zn(NO$_3$)$_2$ concentration (TiO$_2$/ZnO_10mM), a nanosponge-like morphology is mainly observed (Fig. S5a). This morphology is linked with the presence of anatase TiO$_2$. Additionally, particles of different sizes related to ZnO are also present. A mapping of this sample (Fig. S6) shows that, overall, ZnO and TiO$_2$ are closely in contact and only a few areas present TiO$_2$ (or to a lower extent ZnO) without interacting with the other oxide.

TEM images of TiO$_2$/ZnO_30mM (Fig. S5b) show a more sponge-like aspect in which most of TiO$_2$ and ZnO is placed in close contact (see mapping, Fig. 2). It is noteworthy the presence of micropores and cavities in this sample. Additionally, sponge-like structures associated with TiO$_2$ can be observed but to a lesser extent than in TiO$_2$/ZnO_10mM, in agreement with the higher Zn/Ti ratio. In this sample, a few rods of ZnO can be clearly seen (Fig. 2).

Finally, the sample with the highest concentration of Zn(NO$_3$)$_2$ (TiO$_2$/ZnO_60mM) presents a more compact structure (Fig. S5c). A detailed analysis of this sample shows the presence of two main morphologies. The most abundant morphology displays a similar aspect to the one of TiO$_2$/ZnO_30mM, but it is less spongy and with fewer porosity. Additionally, there are a few agglomerations (Fig. S7) in which a high amount of ZnO without interacting with TiO$_2$ is observed.

Interplanar distances were measured on selected particles of these samples in order to determine the Ti or Zn phases formed. Interplanar distances of 1.70, 2.33, 3.52, and 1.89 Å have been observed in all nanostructures, which is a fact associated with the Bragg

13

lines of (105), (112), (101), and (200), respectively, corresponding to tetragonal titania-anatase (JCPDS: 021–1272). Thus, TiO_2 is the only Ti-containing phase detected in these samples. Similarly, the only Zn-containing phase detected is the hexagonal wurtzite ZnO (JCPDS: 036–1451), according to the interplanar distances measured from diffraction rings (2.48, 1.62, 1.38, and 2.60 Å), corresponding to (101), (110), (113) and (002) family planes, respectively. Therefore, apparently, no mixed Ti-Zn-O crystalline phase has been formed although TiO_2 and ZnO entities present, in most cases, a close proximity.

The composition of the samples has been estimated through an EDX analysis of extensive areas (Fig. S8). Apart from the peaks corresponding to Ti, Zn and O, other peaks of C (from the holey carbon film) and Cu (from the cooper grid) were detected. As expected, the Zn/Ti ratio increases with the concentration of the Zn in the electrolyte and the data fits reasonably well with the ratios obtained by EDX-SEM. It is interesting to note that, in spite of the different Zn/Ti ratios observed, a rather homogeneous distribution of titanium and zinc was observed in all the nanostructures. This homogeneous distribution is more marked in the sample with intermediate Zn/Ti ratio (TiO_2/ZnO_30mM), since there is more non-interacting TiO_2 in the sample with less Zn (TiO_2/ZnO_10mM) and more free ZnO can be observed in the sample with a higher Zn/Ti ratio (TiO_2/ZnO_60mM).

3.2.3. Atomic Force Microscopy

Topography of nanostructures was analysed by AFM measurements. Fig. S9 shows, as an example, the topography of TiO_2 nanosponges and TiO_2/ZnO hybrid nanostructures electrodeposited with 30, 40, and 60 mM $Zn(NO_3)_2$. As it can be seen in these images, the samples present a very porous organisation without the presence of dense aggregations. However, more pronounced peaks can be observed for the TiO_2/ZnO hybrid

nanostructures electrodeposited with 40 and 60 mM $Zn(NO_3)_2$, which are associated with a higher roughness.

The morphology observed by AFM is not comparable to the one obtained by FE-SEM because AFM works with a confocal microscope, so the resolution is not as high as that of FE-SEM. However, this technique is very useful because it allows to quantify the roughness of nanostructures. In particular, the roughness of photocatalysts was evaluated from the arithmetic mean height (Sa), and the root mean square (Sq). Table 2 shows the results of Sa and Sq obtained from AFM analysis.

Table 2 shows that the roughness of photocatalysts increases as the ZnO concentration also increases. The greater the amount of electrodeposited ZnO is, the greater the specific area and surface ratio of the nanostructures will be. Both the longitudinal and the transverse growth of the ZnO crystals produce the formation of a ZnO nanostructured layer that sticks out from the surface of the TiO_2 nanosponges. Consequently, the roughness of the samples increases. High roughness values are considered crucial for photoelectrochemical applications, since they make it possible to increase the surface area of nanostructures favouring processes such as photoelectrochemical water splitting [44–46].

According to Table 2, roughness values are similar for TiO_2/ZnO hybrid nanostructures electrodeposited with 10 and 20 mM $Zn(NO_3)_2$ (Sa ≈ 61 nm). The roughness of these nanostructures is about double than the one of TiO_2 nanosponges (Sa ≈ 33 nm). Additionally, with 30 mM $Zn(NO_3)_2$, the roughness increases up to Sa ≈ 80 nm. On the other hand, the relative roughness of the samples obtained with 40 and 50 mM $Zn(NO_3)_2$ is similar (Sa ≈ 130 nm), being more than 50 % higher with respect to those electrodeposited with 30 mM $Zn(NO_3)_2$. Finally, for a concentration of 60 mM $Zn(NO_3)_2$,

the roughness increases more than 300 % (Sa $\approx$ 460 nm) with respect to those electrodeposited with 40 and 50 mM $Zn(NO_3)_2$. Although TiO_2/ZnO hybrid nanostructures electrodeposited at 60 mM $Zn(NO_3)_2$ seem to be apparently compact, the roughness increases substantially due to the presence of ZnO nanochannels that are distributed over the entire surface of photocatalysts.

3.2.4. X-Ray Diffraction

XRD characterisation was carried out to identify the crystalline structure and determine the crystallite size of photocatalysts. Fig. 3 shows, as an example, the XRD pattern of TiO_2/ZnO hybrid nanostructures electrodeposited with 30 mM $Zn(NO_3)_2$.

XRD analysis verified the formation of TiO_2 anatase and ZnO wurtzite phases. On the one hand, the main peak of the tetragonal anatase (101) appears at 25.1º. On the other hand, the main peaks of the hexagonal wurtzite structure appear at 31.6º, 34.2º, and 36.1º and correspond to the crystallographic planes (100), (002), and (101), respectively. In addition, no peaks corresponding to other oxides or ternary compounds were observed, so the formation of ZnO on TiO_2 nanosponges has been carried out successfully. These results are in line with those observed in TEM analysis where Ti-Zn-O mixed phases were not appreciated.

Fig. S10 shows the XRD patterns of TiO_2 nanosponges and TiO_2/ZnO hybrid nanostructures electrodeposited with $Zn(NO_3)_2$ concentrations between 10 and 60 Mm. It is observed that the intensity of the peaks related to ZnO increases as the $Zn(NO_3)_2$ concentration increases, while the intensity of the main peak corresponding to the anatase phase of TiO_2 (101) remains practically constant. This phenomenon takes place due to the differences in the growth rates of the different planes of the crystals that result in

different geometries, sizes, and shapes of crystallite. As mentioned in section 3.1, the different rates of generation of OH$^-$ and diffusion of Zn^{+2} during the electrodeposition process cause differences in the growth rate of ZnO crystals. Therefore, the growth direction of ZnO during the electrodeposition process is affected by the concentration of Zn(NO$_3$)$_2$.

Crystallite sizes of TiO$_2$ and ZnO were calculated using the Scherrer's equation. For this purpose, the main crystallographic planes of the anatase phase of TiO$_2$ (101) and the wurtzite phase of ZnO (101) —25.1º and 36.1º, respectively— were selected. On the one hand, the crystallite size of anatase TiO$_2$ was about 46 nm for all the nanostructures. On the other hand, the crystallite size of wutrzite ZnO changed with the Zn(NO$_3$)$_2$ concentration. Table 3 shows the crystallite sizes of wutrzite ZnO for TiO$_2$/ZnO hybrid nanostructures electrodeposited with Zn(NO$_3$)$_2$ concentrations between 10 and 60 mM.

The crystallite size of ZnO increases as the Zn(NO$_3$)$_2$ concentration increases. The largest crystallite size was obtained with a Zn(NO$_3$)$_2$ concentration of 60 mM (58 nm), while the smallest one was obtained with a concentration of 10 mM (23 nm). Therefore, the variation of Zn(NO$_3$)$_2$ concentration during the electrodeposition process directly influences on the crystallite size.

These results, together with those obtained in the FE-SEM, EDX, and TEM analysis, show that the Zn(NO$_3$)$_2$ concentration affects the amount of electrodeposited ZnO, the morphology of the nanostructures, and the crystallite size of ZnO.

3.2.5. *Ultraviolet–Visible spectroscopy and Band Gap measurements*

UV-Visible spectroscopy was carried out to analyse the ZnO influence on the absorbance of photocatalysts. Fig. 4 shows the UV-Visible absorbance spectra of TiO$_2$ nanosponges

17

and TiO$_2$/ZnO hybrid nanostructures. The spectra of these samples show a similar profile although it has several differences. In all cases, an intense band from 200 to 400 nm followed by a lower intensity band in the 400 to 800 nm region has been observed. However, the addition of ZnO to TiO$_2$ has led to a shift of the 200-400 nm band towards higher wavelengths. This displacement increases with the concentration of ZnO, being very subtle for the sample treated with 10 mM Zn(NO$_3$)$_2$ and notorious for the sample treated with 60 mM Zn(NO$_3$)$_2$. The increase in the absorbance observed in the samples with ZnO is also noteworthy. The higher light absorption intensity observed in the TiO$_2$/ZnO hybrid nanostructures may be related to the formation of heterojunctions at the TiO$_2$/ZnO interface. The introduction of ZnO within TiO$_2$ matrix could produce a narrowing of the band gap, increasing the absorption intensity of the nanostructures. The reduction of the value of the band gap of the TiO$_2$/ZnO hybrid nanostructures could be caused because a new band gap is formed with the valence band of ZnO (less positive than the TiO$_2$ valence band) and the conduction band of TiO$_2$ (less negative than the ZnO conduction band). Therefore, the energy required to excite the electrons of the valence band is reduced [47]. The highest intensity was attained for intermediate ZnO loadings (i.e. 30 mM and 40 mM), whereas further ZnO concentrations led to decreased intensities. Xu et al. [47] related the behaviour of samples with high density of ZnO to the formation of new composite sites that decrease the absorption intensity. Overall, those catalysts with intermediate ZnO loadings present the highest absorption in both ranges —UV and visible— this ease of electron transfer justifies, at least partly, their enhanced photoelectrochemical properties.

Band gaps have also been determined using the Tauc formula [48,49], as shown in Supporting Information, Fig. S11. Pure TiO$_2$ sample presents a band gap width of 3.23 eV (Fig. S11), which is in agreement with what was reported for anatase TiO$_2$ [25,26].

The addition of ZnO leads to a decrease of the width of the band gap (3.06-3.15 eV), which is more remarkable for the nanostructure with the highest ZnO loading. This lower value for the band gap width in Zn-containing samples is in accordance with the red shift observed in the adsorption edge of the UV-Vis spectra. This narrowing of the band gap when ZnO is added takes place in spite of the fact that pure ZnO is a semiconductor with an energy of the band gap of ca. 3.3 eV [27,47], which is even higher than the one of the anatase TiO_2. The fact that the band gap is lower when adding ZnO must be caused by the close interaction of ZnO and TiO_2, creating efficient sites with different electrochemical properties than those of pure ZnO or pure TiO_2.

3.3. Electrochemical and photoelectrochemical characterisation of photocatalysts

Once the structural, compositional, and morphological analysis was completed, an electrochemical and photoelectrochemical characterisation of the nanostructures was carried out. Water splitting and stability tests were used to study the photoelectrochemical performance of the nanostructures and their stability against photocorrosion. These tests determined which nanostructures were the most suitable for photoelectrochemical applications. EIS and Mott-Schottky tests were used to analyse the electrochemical behaviour of the optimal nanostructures.

3.3.1. Photoelectrochemical water splitting and stability tests

Fig. 5. shows the photoelectrochemical tests of TiO_2 nanosponges and TiO_2/ZnO hybrid nanostructures electrodeposited with $Zn(NO_3)_2$ concentrations between 10 and 60 mM. Fig. 5a shows the photoelectrochemical water splitting tests under dark and illuminated (AM 1.5) conditions, and Fig. 5b shows the stability tests to photocorrosion at a potential of 0.84 $V_{Ag/AgCl}$ under illuminated (AM 1.5) conditions.

19

On the one hand, the photoelectrochemical water splitting tests (Fig. 5a) determined that increasing the $Zn(NO_3)_2$ concentration during the electrodeposition process up to 40 mM improves the photoelectrochemical activity of the TiO_2/ZnO hybrid nanostructures. However, the increase of the $Zn(NO_3)_2$ concentration to 50 and 60 mM leads to a reduction in the photoelectrochemical activity of the samples. With TiO_2/ZnO hybrid nanostructures electrodeposited with 40 mM $Zn(NO_3)_2$ ($i = 0.248$ mA·cm^{-2}), it was possible to improve the photoelectrochemical performance up to 343 % compared to TiO_2 nanosponges ($i = 0.056$ mA·cm^{-2}). The influence of the formation of well-defined and structured ZnO nanorods on the entire surface of the TiO_2 nanosponge may be caused by the significant improvement of these nanostructures with respect to the others.

On the other hand, stability tests to photocorrosion (Fig. 5b) determined that TiO_2/ZnO hybrid nanostructures were only stable for $Zn(NO_3)_2$ concentrations lower than 30 mM. The current density drops significantly with $Zn(NO_3)_2$ concentrations higher than 30 mM, so it was determined that these nanostructures were not stable.

Based on the results obtained in these experiments, it could be seen that the optimal nanostructures to carry out photoelectrochemical applications were the TiO_2/ZnO hybrid nanostructures electrodeposited with a $Zn(NO_3)_2$ concentration of 30 mM ($i = 0.170$ mA·cm^{-2}). These nanostructures were stable against photocorrosion and they offered an improvement of 204 % in photoelectrochemical activity compared to TiO_2 nanosponges.

3.3.2. Electrochemical impedance spectroscopy

The kinetics of the electrochemical and photoelectrochemical processes have been studied by electrochemical impedance spectroscopy (EIS). In order to do it, TiO_2/ZnO hybrid nanostructures that offered the best results during water splitting and stability tests to photocorrosion were selected, that is, TiO_2/ZnO hybrid nanostructures electrodeposited

20

with 30 mM $Zn(NO_3)_2$. For comparison, EIS tests were also performed with ZnO-free TiO_2 nanosponges.

Fig. 6 shows Nyquist plots obtained at a potential of 0.6 $V_{Ag/AgCl}$ in dark and illuminated conditions for TiO_2 nanosponges and TiO_2/ZnO hybrid nanosponges electrodeposited with a $Zn(NO_3)_2$ concentration of 30 mM.

Semicircles observed in the Nyquist plot are related to the charge transfer resistance of the nanostructures [30,33,50]. Two facts can be drawn from Fig. 6. First, the impedance values are much lower under illuminated than under dark conditions because electrons in the valence band are excited towards the conduction band under illuminated conditions, increasing the conductivity of nanostructures and the transport of electrons and holes. Second, TiO_2/ZnO hybrid nanosponges electrodeposited with 30 mM $Zn(NO_3)_2$ show a considerably lower charge transfer resistance than TiO_2 nanosponges. The interconnection of the valence and conduction bands of TiO_2 and ZnO can lead to a greater electronic transport and a better charge separation [51].

Fig. 7 shows the Bode modulus and the Bode phase plots obtained at 0.6 $V_{Ag/AgCl}$ in dark and illuminated conditions for TiO_2 nanosponges and TiO_2/ZnO hybrid nanosponges electrodeposited with a $Zn(NO_3)_2$ concentration of 30 mM.

On the one hand, in the Bode modulus plot (Fig. 7a), three different factors can be appreciated. First, at high frequencies ($10^3 - 10^5$ Hz) no differences are shown regardless of the composition of the nanostructures or the illumination conditions. The impedance modulus at high frequencies is related to the resistance of the electrolyte. This resistance is similar in all cases because the electrolyte is the same. Second, the impedance modulus of both nanostructures decreases under illuminated conditions at low frequencies ($10^{-2} - 1$ Hz) due to a higher conductivity of the nanostructures caused by the photoexcited

21

electrons. Finally, it can be observed that the total impedance of the system is lower for TiO$_2$/ZnO hybrid nanosponges. Therefore, as mentioned above, the charge transfer resistance decreases in comparison to TiO$_2$ nanosponges, which results in an improvement in the electrochemical and photoelectrochemical properties of TiO$_2$/ZnO hybrid nanosponges, as it has been corroborated in water splitting tests.

On the other hand, a broad peak can be observed in the Bode phase plots (Fig. 7b), which corresponds to the superposition of two peaks related to the existence of two different time constants. There is a shift of the peaks towards lower frequency values for TiO$_2$/ZnO hybrid nanosponges, which indicates longer charge lifetime [33,52]. Electron lifetimes can be calculated according to the following formula $\tau = 1/(2 \cdot \pi \cdot f_{max})$, where f_{max} is the frequency of the maximum value of the peak of the Bode phase plot. Under illuminated conditions, the electron lifetime of TiO$_2$ nanosponges is 0.43 ms, while it is 85.47 ms for the TiO$_2$/ZnO hybrid nanosponges. It can be seen then that, by using TiO$_2$/ZnO hybrid nanosponges, a greater number of electrochemical reactions will be carried out and, therefore, the photoelectrochemical performance of these photoelectrodes will be considerably higher.

Fig. S12 shows the results of impedance modulus (|Z|) for TiO$_2$ nanosponges and TiO$_2$/ZnO hybrid nanosponges electrodeposited with a Zn(NO$_3$)$_2$ concentration of 30 mM under dark and illuminated conditions.

In Fig. S12 it can be seen that for both TiO$_2$ nanosponges and TiO$_2$/ZnO hybrid nanosponges, the charge transfer resistance decreases considerably under illuminated conditions compared to dark conditions due to an increase in the electrical conductivity of the nanostructures, leading to a better electron transfer. Photogenerated electrons cause an increase in the electrical conductivity of nanostructures. In addition, for TiO$_2$/ZnO

22

hybrid nanosponges electrodeposited with a Zn(NO$_3$)$_2$ concentration of 30 mM, the charge transfer resistance decreases both in dark and illuminated conditions compared to TiO$_2$ nanosponges. This decrease may happen due to the fact that TiO$_2$/ZnO hybrid nanostructures have a greater number of defects as a consequence of the introduction of ZnO into the nanostructures, obtaining a more efficient charge separation and a greater number of charge carriers [30,33,50,52,53].

3.3.3. Mott-Schottky tests

Mott-Schottky analysis was performed under illuminated and dark conditions for TiO$_2$ nanosponges and TiO$_2$/ZnO hybrid nanosponges electrodeposited with a Zn(NO$_3$)$_2$ concentration of 30 mM. This technique makes it possible to analyse the electrochemical capacitance at the semiconductor/electrolyte interface of the nanostructures, being able to calculate the charge carriers density according to the Mott-Schottky equation:

$$\frac{1}{Csc^2} = \frac{2}{e \cdot \varepsilon \cdot \varepsilon_0 \cdot N_D} \cdot \left(U - U_{FB} - \frac{k \cdot T}{e} \right) \qquad \text{Eq. 2}$$

C_{SC} is the capacitance of the space charge region, e the electron charge (1.6·10^{-19} C), ε the dielectric constant of TiO$_2$ (100 [12,54]) and TiO$_2$/ZnO (78, calculated from the weighted volume value and the dielectric constant of TiO$_2$ and ZnO (10 [31,55])), ε_0 the permittivity vacuum (8.85·10^{-14} F/cm), N_D the donor density, U is applied potential difference, U_{FB} the flat-band potential, k the Boltzman constant (1.38·10^{-23} J/K), and T is the absolute temperature.

Fig 10 shows the Mott-Schottky plots from 0.8 to -0.9 V$_{Ag/AgCl}$ at a frequency of 10 kHz under illuminated and dark conditions for TiO$_2$ nanosponges and TiO$_2$/ZnO hybrid nanostructures electrodeposited with 30 mM Zn(NO$_3$)$_2$.

23

Fig. 8 shows a positive slope for all the nanostructures, confirming the n-type semiconductor characteristics, where the donor density is associated with electrons [31–33]. The capacitance values of the hybrid nanostructures are higher than those of the TiO$_2$ nanosponges (lower values of C_{SC}^{-2}), and they are also higher under illuminated conditions. It is possible to obtain the donor density (N_D) from Fig. 8. Table 4 shows N_D under dark and illuminated conditions for TiO$_2$ nanosponges and TiO$_2$/ZnO hybrid nanostructures electrodeposited with 30 mM Zn(NO$_3$)$_2$.

Table 4 also shows that N_D values slightly increase when changing from dark to illuminated conditions, both in TiO$_2$ nanosponges and TiO$_2$/ZnO hybrid nanostructures. Under illumination, electrons are excited from the valence band to the conduction band, increasing the amount of charge carriers. On the other hand, N_D is considerably higher in TiO$_2$/ZnO hybrid nanostructures than in TiO$_2$ nanosponges. The increase of N_D may be related to a greater number of defects produced by the introduction of ZnO into the TiO$_2$ matrix, thus improving the charge transfer of the nanostructures. These results are in agreement with those obtained in the EIS analysis. The improvement in charge separation added to lower resistance to charge transfer makes the TiO$_2$/ZnO hybrid nanostructures more favourable than TiO$_2$ nanosponges for photoelectrochemical applications.

4.   Conclusions

The morphology, properties and composition of TiO$_2$/ZnO hybrid nanostructures were controlled by modifying the Zn(NO$_3$)$_2$ concentration during the electrodeposition process. A nanosponge morphology was observed for Zn(NO$_3$)$_2$ concentrations from 10 mM to 30 mM. However, at higher Zn(NO$_3$)$_2$ concentrations, the morphology of the nanostructures significantly changed. First, a uniform morphology composed of well-defined ZnO hexagonal nanorods was observed with 40 mM Zn(NO$_3$)$_2$. Second, nanostructures

24

covered by ZnO with undefined nanorods were observed using 50 mM $Zn(NO_3)_2$. Finally, for a $Zn(NO_3)_2$ concentration of 60 mM, a nanostructure composed of ZnO nanoplates with separated clusters sticking out from the surface was observed. In addition, it was determined that by increasing the $Zn(NO_3)_2$ concentration, the amount of electrodeposited ZnO, the roughness and the crystallite size of ZnO increased, and the band gap decreased.

The photocatalysts that showed the best photocatalytic activity were the TiO_2/ZnO hybrid nanostructures electrodeposited with 40 mM $Zn(NO_3)_2$ (343 % higher than TiO_2 nanosponges), but they were not stable against photocorrosion. So, the TiO_2/ZnO hybrid nanostructures electrodeposited with 30 mM $Zn(NO_3)_2$ were selected as the most favourable photocatalysts because they were stable against photocorrosion and offered a high photoelectrochemical performance (204 % higher than TiO_2 nanosponges). In addition, EIS and Mott-Schottky tests showed that they presented a lower resistance to charge transfer and a higher donor density compared to TiO_2 nanosponges.

The best performance of the sample with a medium Zn-loading, 30 mM $Zn(NO_3)_2$, must be due to the close interaction between TiO_2 and ZnO, which improves the electronic properties with a scarce formation of non-interacting ZnO, which is highly unstable.

25

References

[1]   M. Ahmed, I. Dincer, A review on photoelectrochemical hydrogen production systems: Challenges and future directions, Int. J. Hydrogen Energy. 44 (2019) 2474–2507. doi:10.1016/j.ijhydene.2018.12.037.

[2]   Z. Liu, B. Pesic, K.S. Raja, R.R. Rangaraju, M. Misra, Hydrogen generation under sunlight by self ordered TiO2 nanotube arrays, Int. J. Hydrogen Energy. 34 (2009) 3250–3257. doi:10.1016/j.ijhydene.2009.02.044.

[3]   K. Maeda, K. Domen, Photocatalytic water splitting: Recent progress and future challenges, J. Phys. Chem. Lett. 1 (2010) 2655–2661. doi:10.1021/jz1007966.

[4]   X. He, Y. Cai, H. Zhang, C. Liang, Photocatalytic degradation of organic pollutants with Ag decorated free-standing TiO2 nanotube arrays and interface electrochemical response, J. Mater. Chem. 21 (2011) 475–480. doi:10.1039/c0jm02404j.

[5]   D. Chen, Y. Cheng, N. Zhou, P. Chen, Y. Wang, K. Li, S. Huo, P. Cheng, P. Peng, R. Zhang, L. Wang, H. Liu, Y. Liu, R. Ruan, Photocatalytic degradation of organic pollutants using TiO2-based photocatalysts: A review, J. Clean. Prod. 268 (2020) 121725. doi:10.1016/j.jclepro.2020.121725.

[6]   H. Jiang, H. Dai, X. Meng, L. Zhang, J. Deng, K. Ji, Morphology-dependent photocatalytic performance of monoclinic BiVO4 for methyl orange degradation

under visible-light irradiation, Cuihua Xuebao/Chinese J. Catal. 32 (2011) 939–949. doi:10.1016/S1872-2067(10)60215-X.

[7]   D. Regonini, C.R. Bowen, A. Jaroenworaluck, R. Stevens, A review of growth mechanism, structure and crystallinity of anodized TiO2 nanotubes, Mater. Sci. Eng. R Reports. 74 (2013) 377–406. doi:10.1016/j.mser.2013.10.001.

[8]   A. Kumar, Different Methods Used for the Synthesis of TiO2 Based Nanomaterials: A Review, Am. J. Nano Res. Appl. 6 (2018) 1. doi:10.11648/j.nano.20180601.11.

[9]   W. Guo, F. Zhang, C. Lin, Z.L. Wang, Direct growth of TiO2 nanosheet arrays on carbon fibers for highly efficient photocatalytic degradation of methyl orange, Adv. Mater. 24 (2012) 4761–4764. doi:10.1002/adma.201201075.

[10]   R. Sánchez-Tovar, R.M. Fernández-Domene, D.M. García-García, J. García-Antón, Enhancement of photoelectrochemical activity for water splitting by controlling hydrodynamic conditions on titanium anodization, J. Power Sources. 286 (2015) 224–231. doi:10.1016/j.jpowsour.2015.03.174.

[11]   J. Harris, R. Silk, M. Smith, Y. Dong, W.T. Chen, G.I.N. Waterhouse, Hierarchical TiO2Nanoflower Photocatalysts with Remarkable Activity for Aqueous Methylene Blue Photo-Oxidation, ACS Omega. 5 (2020) 18919–18934. doi:10.1021/acsomega.0c02142.

[12]   L. Aïnouche, L. Hamadou, A. Kadri, N. Benbrahim, D. Bradai, Interfacial barrier layer properties of three generations of TiO 2 nanotube arrays, Electrochim. Acta. 133 (2014) 597–609. doi:10.1016/j.electacta.2014.04.086.

[13]   Y. Lai, H. Zhuang, L. Sun, Z. Chen, C. Lin, Self-organized TiO2 nanotubes in

mixed organic-inorganic electrolytes and their photoelectrochemical

performance, Electrochim. Acta. 54 (2009) 6536–6542.

doi:10.1016/j.electacta.2009.06.029.

[14]   P. Roy, S. Berger, P. Schmuki, TiO2 nanotubes: Synthesis and applications,

Angew. Chemie - Int. Ed. 50 (2011) 2904–2939. doi:10.1002/anie.201001374.

[15]   S. Reghunath, D. Pinheiro, S.D. KR, A review of hierarchical nanostructures of

TiO2: Advances and applications, Appl. Surf. Sci. Adv. 3 (2021) 100063.

doi:10.1016/j.apsadv.2021.100063.

[16]   E. Blasco-Tamarit, M.J. Muñoz-Portero, R. Sánchez-Tovar, R.M. Fernández-

Domene, J. García-Antón, The effect of Reynolds number on TiO2 nanosponges

doped with Li+ cations, New J. Chem. 42 (2018) 11054–11063.

doi:10.1039/c8nj00800k.

[17]   R. Sánchez-Tovar, E. Blasco-Tamarit, R.M. Fernández-Domene, B. Lucas-

Granados, J. García-Antón, Should TiO2 nanostructures doped with Li+ be used

as photoanodes for photoelectrochemical water splitting applications?, J. Catal.

349 (2017) 41–52. doi:10.1016/j.jcat.2017.03.001.

[18]   R.M. Fernández-Domene, R. Sánchez-Tovar, S. Sánchez-González, J. García-

Antón, Photoelectrochemical characterization of anatase-rutile mixed TiO2

nanosponges, Int. J. Hydrogen Energy. 41 (2016) 18380–18388.

doi:10.1016/j.ijhydene.2016.08.012.

[19]   G.K. Mor, O.K. Varghese, M. Paulose, K. Shankar, C.A. Grimes, A review on

highly ordered, vertically oriented TiO2 nanotube arrays: Fabrication, material

properties, and solar energy applications, Sol. Energy Mater. Sol. Cells. 90 (2006) 2011–2075. doi:10.1016/j.solmat.2006.04.007.

[20]   O. Rosseler, M. V. Shankar, M.K. Le Du, L. Schmidlin, N. Keller, V. Keller, Solar light photocatalytic hydrogen production from water over Pt and Au/TiO2(anatase/rutile) photocatalysts: Influence of noble metal and porogen promotion, J. Catal. 269 (2010) 179–190. doi:10.1016/j.jcat.2009.11.006.

[21]   K. Aijo John, J. Naduvath, S.K. Remillard, S. Shaji, P.A. DeYoung, Z.T. Kellner, S. Mallick, M. Thankamoniamma, G.S. Okram, R.R. Philip, A simple method to fabricate metal doped TiO 2 nanotubes, Chem. Phys. 523 (2019) 198–204. doi:10.1016/j.chemphys.2019.04.028.

[22]   L.G. Devi, B.N. Murthy, S.G. Kumar, Photocatalytic activity of TiO2 doped with Zn2+ and V5+ transition metal ions: Influence of crystallite size and dopant electronic configuration on photocatalytic activity, Mater. Sci. Eng. B Solid-State Mater. Adv. Technol. 166 (2010) 1–6. doi:10.1016/j.mseb.2009.09.008.

[23]   K.R. Reddy, M. Hassan, V.G. Gomes, Hybrid nanostructures based on titanium dioxide for enhanced photocatalysis, Appl. Catal. A Gen. 489 (2015) 1–16. doi:10.1016/j.apcata.2014.10.001.

[24]   J. Zhang, G. Xiao, F.X. Xiao, B. Liu, Revisiting one-dimensional TiO2 based hybrid heterostructures for heterogeneous photocatalysis: A critical review, Mater. Chem. Front. 1 (2017) 231–250. doi:10.1039/c6qm00141f.

[25]   M.J. Jin, J. Jo, J.H. Kim, K.S. An, M.S. Jeong, J. Kim, J.W. Yoo, Effects of TiO2 interfacial atomic layers on device performances and exciton dynamics in ZnO nanorod polymer solar cells, ACS Appl. Mater. Interfaces. 6 (2014) 11649–

29

11656. doi:10.1021/am5024435.

[26] D. Reyes-Coronado, G. Rodríguez-Gattorno, M.E. Espinosa-Pesqueira, C. Cab, R. De Coss, G. Oskam, Phase-pure TiO2 nanoparticles: Anatase, brookite and rutile, Nanotechnology. 19 (2008). doi:10.1088/0957-4484/19/14/145605.

[27] D. Guo, J. Wang, C. Cui, P. Li, X. Zhong, F. Wang, S. Yuan, K. Zhang, Y. Zhou, ZnO@TiO2 core-shell nanorod arrays with enhanced photoelectrochemical performance, Sol. Energy. 95 (2013) 237–245. doi:10.1016/j.solener.2013.06.003.

[28] W.H. Lin, Y.H. Chiu, P.W. Shao, Y.J. Hsu, Metal-Particle-Decorated ZnO Nanocrystals: Photocatalysis and Charge Dynamics, ACS Appl. Mater. Interfaces. 8 (2016) 32754–32763. doi:10.1021/acsami.6b08132.

[29] J. Lu, H. Jin, Y. Dai, K. Yang, B. Huang, Effect of electronegativity and charge balance on the visible-light- responsive photocatalytic activity of nonmetal doped anatase TiO 2, Int. J. Photoenergy. 2012 (2012). doi:10.1155/2012/928503.

[30] S. Hernández, D. Hidalgo, A. Sacco, A. Chiodoni, A. Lamberti, V. Cauda, E. Tresso, G. Saracco, Comparison of photocatalytic and transport properties of TiO2 and ZnO nanostructures for solar-driven water splitting, Phys. Chem. Chem. Phys. 17 (2015) 7775–7786. doi:10.1039/c4cp05857g.

[31] C.C. Wang, C.Y. Chou, S.R. Yi, H.D. Chen, Deposition of heterojunction of ZnO on hydrogenated TiO2 nanotube arrays by atomic layer deposition for enhanced photoelectrochemical water splitting, Int. J. Hydrogen Energy. 44 (2019) 28685–28697. doi:10.1016/j.ijhydene.2019.09.133.

[32] K.P. Shejale, D. Laishram, R. Gupta, R.K. Sharma, Engineered ZnO-TiO2 Nanospheres for High Performing Membrane Assimilated Photocatalytic Water Remediation and Energy Harvesting, ChemistrySelect. 3 (2018) 7291–7301. doi:10.1002/slct.201800988.

[33] F. Xu, J. Mei, X. Li, Y. Sun, D. Wu, Z. Gao, Q. Zhang, K. Jiang, Heterogeneous three-dimensional TiO2/ZnO nanorod array for enhanced photoelectrochemical water splitting properties, J. Nanoparticle Res. 19 (2017). doi:10.1007/s11051-017-3982-8.

[34] C.C. Wang, C.Y. Chou, S.R. Yi, H.D. Chen, Deposition of heterojunction of ZnO on hydrogenated TiO2 nanotube arrays by atomic layer deposition for enhanced photoelectrochemical water splitting, Int. J. Hydrogen Energy. 44 (2019) 28685–28697. doi:10.1016/j.ijhydene.2019.09.133.

[35] W. Liu, P. Su, S. Chen, N. Wang, Y. Ma, Y. Liu, J. Wang, Z. Zhang, H. Li, T.J. Webster, Synthesis of TiO2 nanotubes with ZnO nanoparticles to achieve antibacterial properties and stem cell compatibility, Nanoscale. 6 (2014) 9050–9062. doi:10.1039/c4nr01531b.

[36] Y. Liao, K. Zhang, X. Wang, D. Zhang, Y. Li, H. Su, H. Zhang, Z. Zhong, Preparation of ZnO@TiO2 nanotubes heterostructured film by thermal decomposition and their photocatalytic performances, RSC Adv. 8 (2018) 8064–8070. doi:10.1039/c7ra13222k.

[37] K. Pugazhendhi, S. D'Almeida, P.N. Kumar, J.S.S. Mary, T. Tenkyong, D.J. Sharmila, M. J, J.M. Shyla, Hybrid TiO 2 /ZnO and TiO 2 /Al plasmon impregnated ZnO nanocomposite photoanodes for DSSCs: synthesis and

characterisation , Mater. Res. Express. 5 (2018) 045053. doi:10.1088/2053-1591/aab7af.

[38] N.K. Perkgoz, R.S. Toru, E. Unal, M.A. Sefunc, S. Tek, E. Mutlugun, I.M. Soganci, H. Celiker, G. Celiker, H.V. Demir, Photocatalytic hybrid nanocomposites of metal oxide nanoparticles enhanced towards the visible spectral range, Appl. Catal. B Environ. 105 (2011) 77–85. doi:10.1016/j.apcatb.2011.03.037.

[39] C. Yilmaz, U. Unal, Effect of Zn(NO 3)2 concentration in hydrothermal-electrochemical deposition on morphology and photoelectrochemical properties of ZnO nanorods, Appl. Surf. Sci. 368 (2016) 456–463. doi:10.1016/j.apsusc.2016.01.253.

[40] S. Otani, J. Katayama, H. Umemoto, M. Matsuoka, Effect of Bath Temperature on the Electrodeposition Mechanism of Zinc Oxide Film from Zinc Nitrate Solution, J. Electrochem. Soc. 153 (2006) C551. doi:10.1149/1.2205187.

[41] M. Eyraud, G. Jimenez-Cadena, C. Chassigneux, F. Vacandio, E. Comini, G. Sberveglieri, T. Djenizian, Electrochemical fabrication of oriented ZnO nanorods on TiO2 nanotubes, Int. J. Nanotechnol. 9 (2012) 295–311. doi:10.1504/IJNT.2012.045333.

[42] R. Sánchez-Tovar, E. Blasco-Tamarit, R.M. Fernández-Domene, M. Villanueva-Pascual, J. García-Antón, Electrochemical formation of novel TiO2-ZnO hybrid nanostructures for photoelectrochemical water splitting applications, Surf. Coatings Technol. 388 (2020) 125605. doi:10.1016/j.surfcoat.2020.125605.

[43] A. Rey, P. García-Muñoz, M.D. Hernández-Alonso, E. Mena, S. García-

Rodríguez, F.J. Beltrán, WO3-TiO2 based catalysts for the simulated solar radiation assisted photocatalytic ozonation of emerging contaminants in a municipal wastewater treatment plant effluent, Appl. Catal. B Environ. 154–155 (2014) 274–284. doi:10.1016/j.apcatb.2014.02.035.

[44] M. Skompska, K. Zarebska, Electrodeposition of ZnO Nanorod Arrays on Transparent Conducting Substrates–a Review, Electrochim. Acta. 127 (2014) 467–488. doi:10.1016/j.electacta.2014.02.049.

[45] N.S. Zulkiflee, R. Hussin, J. Halim, M.I. Ibrahim, M.Z. Zainal, S. Nizam, S.A. Rahman, Characterization of TiO2, ZnO, and TiO2/ZnO thin films prepared by sol-gel method, ARPN J. Eng. Appl. Sci. 11 (2016) 7633–7637.

[46] N. Naseri, M. Yousefi, A.Z. Moshfegh, A comparative study on photoelectrochemical activity of ZnO/TiO2 and TiO2/ZnO nanolayer systems under visible irradiation, Sol. Energy. 85 (2011) 1972–1978. doi:10.1016/j.solener.2011.05.002.

[47] K. Xu, Z. Liu, S. Qi, Z. Yin, S. Deng, M. Zhang, Z. Sun, The quaternary system of Ag2S/ZnS co-modified ZnO/TiO2 nanotree arrays: Excellent photocatalysis and photoelectrochemistry performance, Appl. Surf. Sci. 538 (2021). doi:10.1016/j.apsusc.2020.148044.

[48] J. Tauc, R. Grigorovici, A. Vancu, Optical Properties and Electronic Structure of Amorphous Germanium, Phys. Status Solidi. 15 (1966) 627–637. doi:https://doi.org/10.1002/pssb.19660150224.

[49] H. Fritzsche, Electronic Processes in Non-Crystalline Materials. N. F. Mott and E. A. Davis. Oxford University Press, New York, 1971. xiv, 438 pp., illus. $24.

33

International Series of Monographs on Physics, Science (80-.). 176 (1972) 1117. doi:10.1126/science.176.4039.1117.

[50] M. Pavlenko, K. Siuzdak, E. Coy, K. Załęski, M. Jancelewicz, I. Iatsunskyi, Enhanced solar-driven water splitting of 1D core-shell Si/TiO2/ZnO nanopillars, Int. J. Hydrogen Energy. 45 (2020) 26426–26433. doi:10.1016/j.ijhydene.2019.11.231.

[51] S. Hernández, V. Cauda, A. Chiodoni, S. Dallorto, A. Sacco, D. Hidalgo, E. Celasco, C.F. Pirri, Optimization of 1D ZnO@TiO2 core-shell nanostructures for enhanced photoelectrochemical water splitting under solar light illumination, ACS Appl. Mater. Interfaces. 6 (2014) 12153–12167. doi:10.1021/am501379m.

[52] H.L. Feng, W.Q. Wu, H.S. Rao, Q. Wan, L. Bin Li, D. Bin Kuang, C.Y. Su, Three-dimensional TiO2/ZnO hybrid array as a heterostructured anode for efficient quantum-dot-sensitized solar cells, ACS Appl. Mater. Interfaces. 7 (2015) 5199–5205. doi:10.1021/am507983y.

[53] D. Wang, J. Ni, J. Guan, X. Zhou, S. Zhang, Y. Zhang, Q. Huang, H. Cai, J. Li, J. Zhang, Thin Film of TiO2-ZnO Binary Mixed Nanoparticles as Electron Transport Layers in Low-Temperature Processed Perovskite Solar Cells, Nano. 15 (2020) 1–10. doi:10.1142/S1793292020500368.

[54] J. Borràs-Ferrís, R. Sánchez-Tovar, E. Blasco-Tamarit, R.M. Fernández-Domene, J. García-Antón, Effect of Reynolds number and lithium cation insertion on titanium anodization, Electrochim. Acta. 196 (2016) 24–32. doi:10.1016/j.electacta.2016.02.160.

[55] I. Mora-Seró, F. Fabregat-Santiago, B. Denier, J. Bisquert, R. Tena-Zaera, J.

Elias, C. Lévy-Clément, Determination of carrier density of ZnO nanowires by electrochemical techniques, Appl. Phys. Lett. 89 (2006) 18–21. doi:10.1063/1.2390667.

Figure Captions

Fig. 1. FE-SEM images of the surface of TiO_2/ZnO hybrid nanostructures.

Fig. 2. Transmission electron microscopy image of TiO_2/ZnO hybrid nanostructures electrodeposited with 30mM $Zn(NO_3)_2$ with the corresponding EDX mapping. Two additional high-resolution TEM images are also included.

Fig. 3. XRD pattern of TiO_2/ZnO hybrid nanostructures electrodeposited with 30 mM $Zn(NO_3)_2$.

Fig. 4. UV-Visible absorption spectra for TiO_2 nanosponges and TiO_2/ZnO hybrid nanostructures.

Fig. 5. (a) Photoelectrochemical water splitting test under dark and iluminated conditions (AM 1.5), and (b) stability tests to photocorrosion at 0.84 $V_{Ag/AgCl}$ under illuminated conditions, for TiO_2 nanosponges and TiO_2/ZnO hybrid nanostructures electrodeposited with different $Zn(NO_3)_2$ concentrations.

Fig. 6. (a) Experimental Nyquist plot obtained at a potential of 0.6 $V_{Ag/AgCl}$ in dark and illuminated conditions for the TiO_2 nanosponges and the TiO_2/ZnO hybrid nanosponges electrodeposited with 30 mM $Zn(NO_3)_2$. (b) Magnification of Experimental Nyquist plot.

Fig. 7. Experimental Bode plots of (a) modulus and (b) phase, obtained at a potential of 0.6 $V_{Ag/AgCl}$ in dark and illuminated conditions for the TiO_2 nanosponges and the TiO_2/ZnO hybrid nanosponges electrodeposited with 30 mM $Zn(NO_3)_2$.

Fig. 8. Mott-Schottky plots obtained at 10 kH under illuminated and dark conditions for TiO_2 nanosponges and TiO_2/ZnO hybrid nanostructures electrodeposited with 30 mM $Zn(NO_3)_2$.
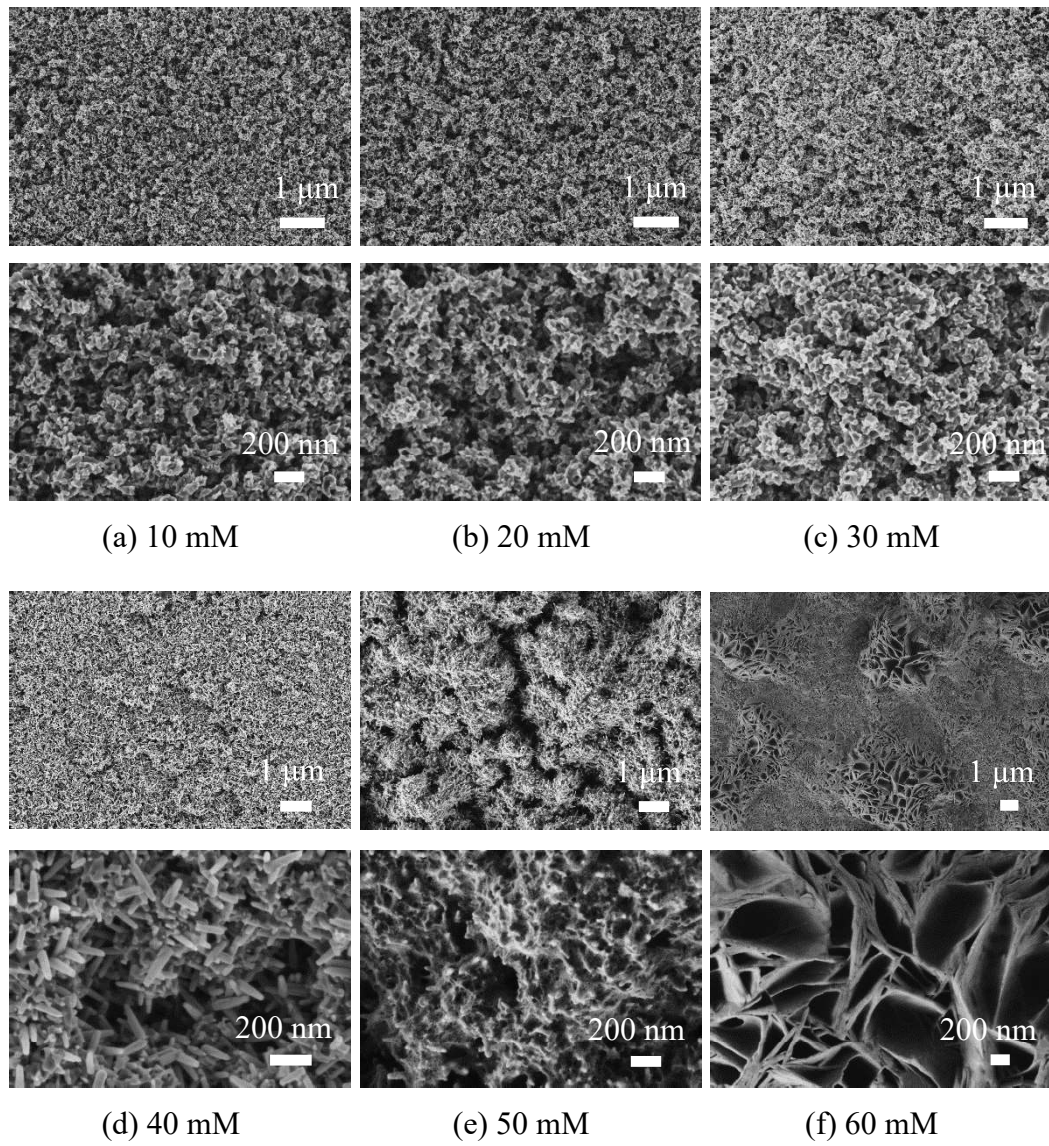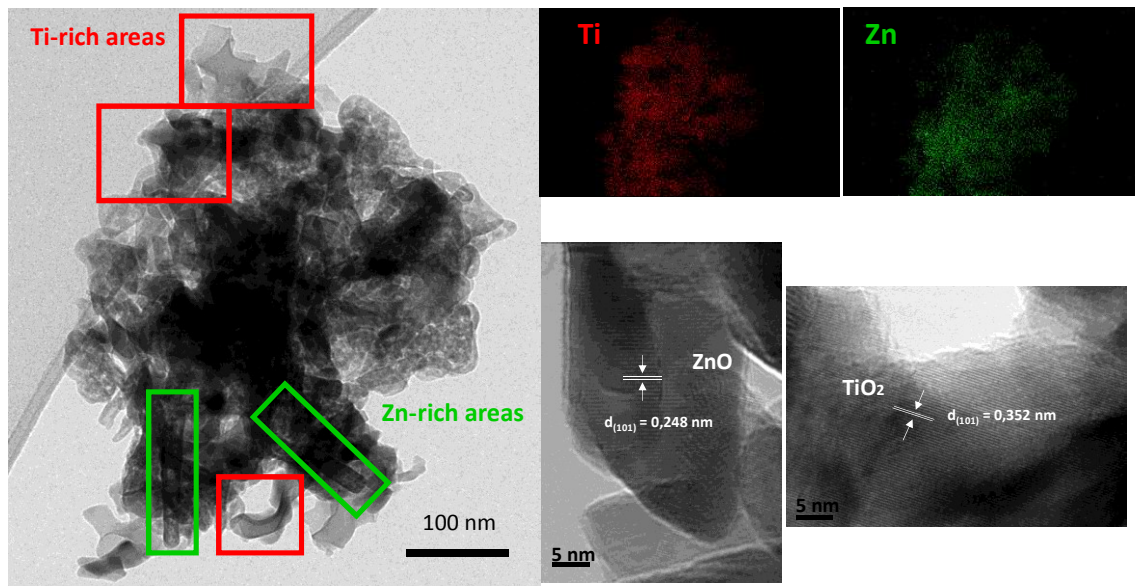
Table captions

Table 1. EDX analysis of the TiO_2 nanosponges and TiO_2/ZnO hybrid nanostructures electrodeposited at 75 ºC.
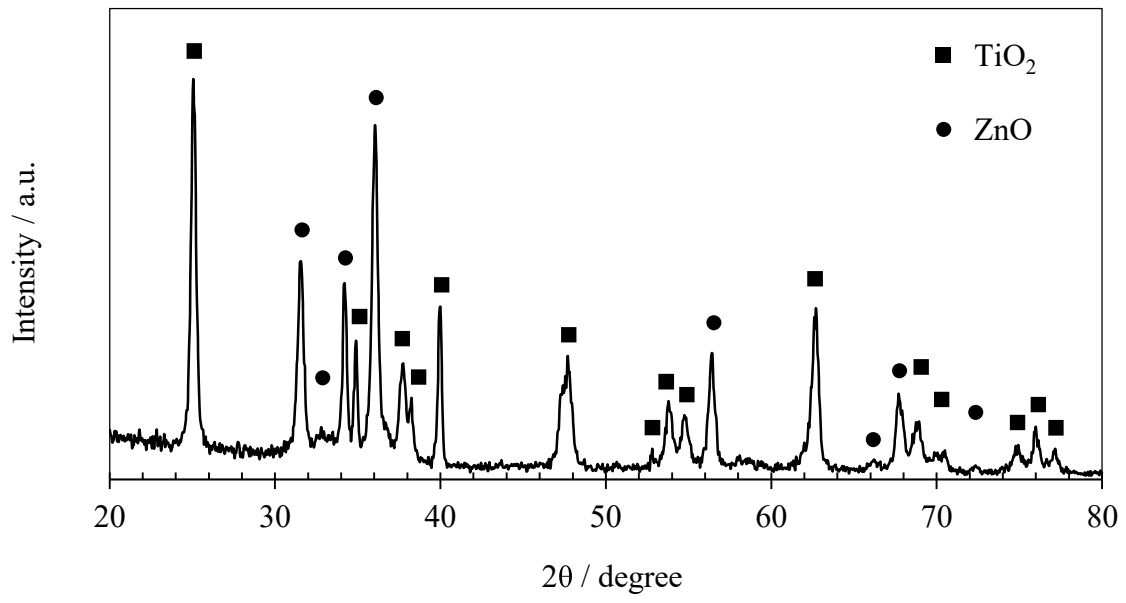
Table 2. Arithmetic mean height (Sa), and root mean square (Sq) of the TiO_2 nanosponges and the TiO_2/ZnO hybrid nanostructures obtained by AFM.

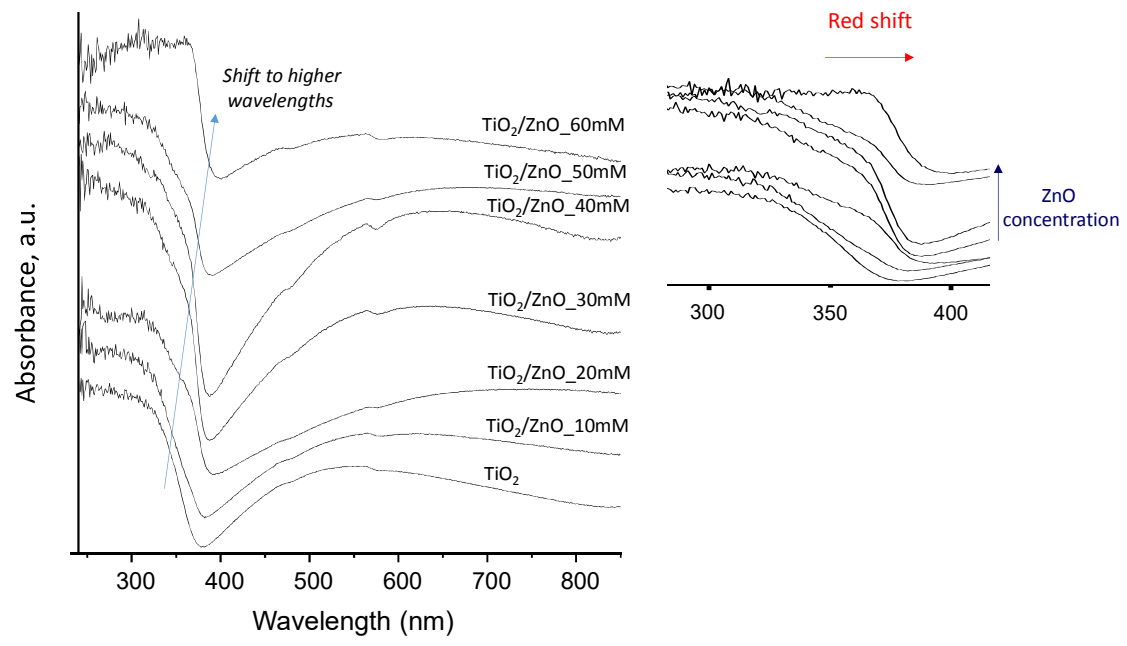**Table 3**. Crystallite sizes of wutrzite ZnO for the TiO_2/ZnO hybrid nanostructures.

Table 4. Donor density of TiO_2 nanosponges and TiO_2/ZnO hybrid nanostructures electrodeposited with 30 mM $Zn(NO_3)_2$.
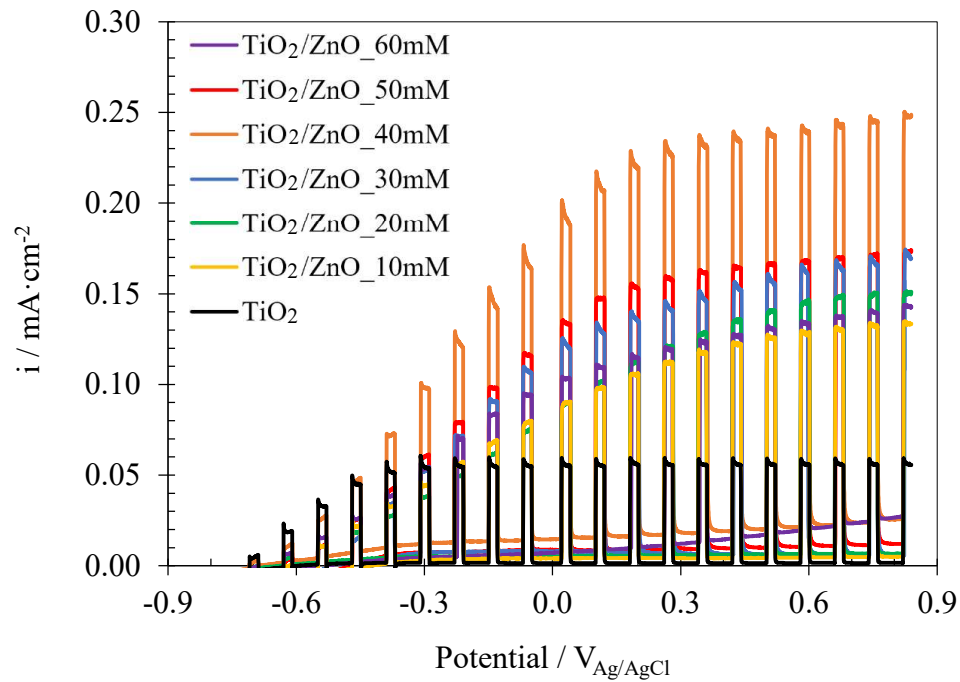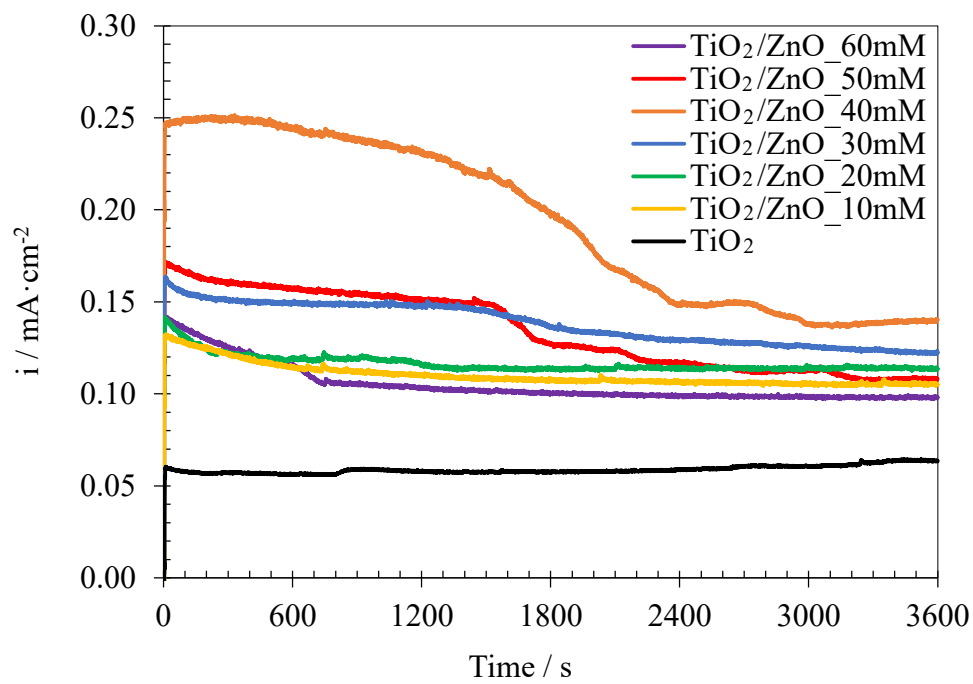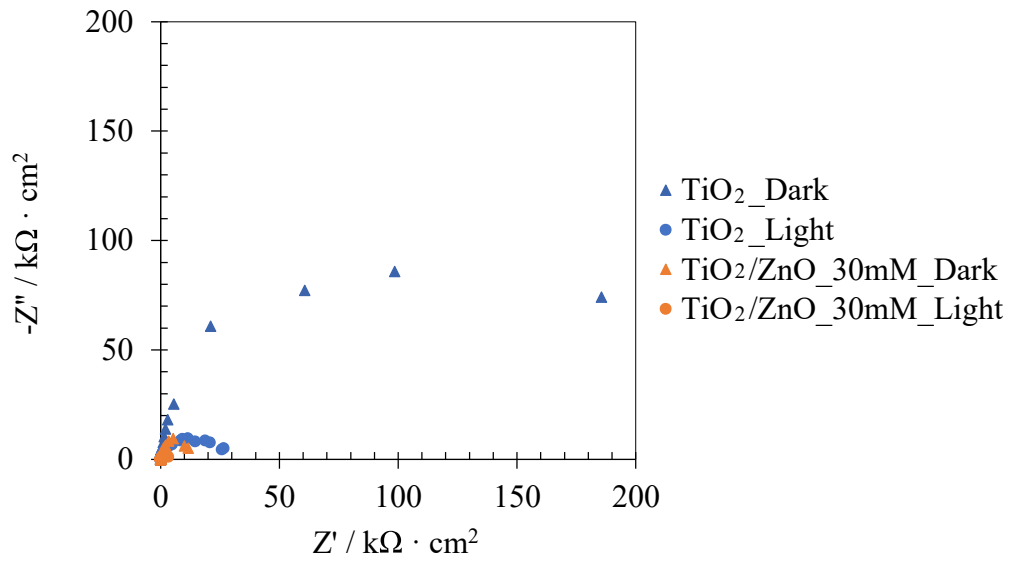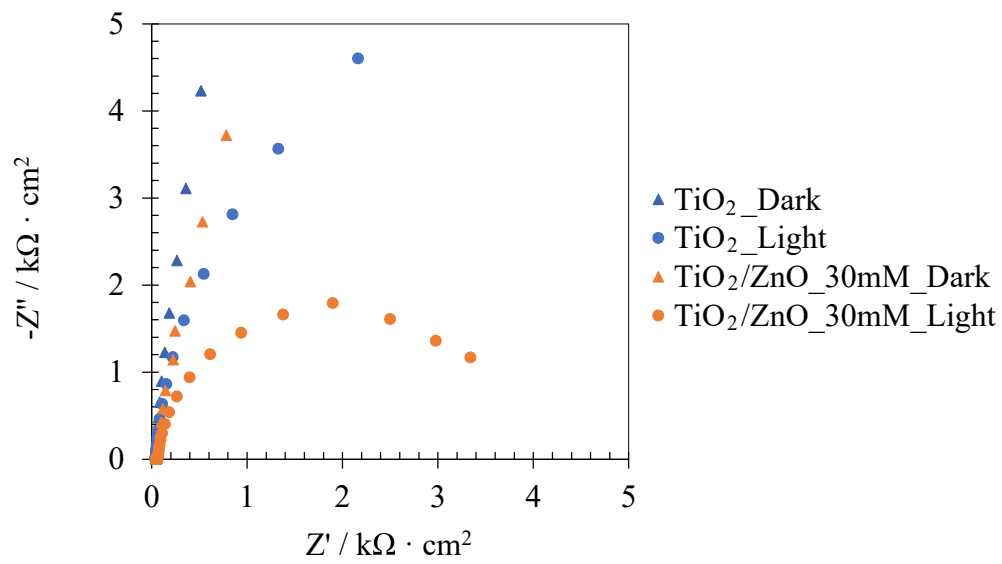
Figure 1
Click here to access/download;Figure;Figure 1.docx ⬇

(a) 10 mM   (b) 20 mM   (c) 30 mM

(d) 40 mM   (e) 50 mM   (f) 60 mM

Figure 3

Figure 4

Figure 5   Click here to access/download;Figure;Figure 5.docx ⬇

(a)

(a)

Figure 6   Click here to access/download;Figure;Figure 6.docx ⬇

(a)

(b)

Figure 7

(a)

(b)

Figure 8

Table 1
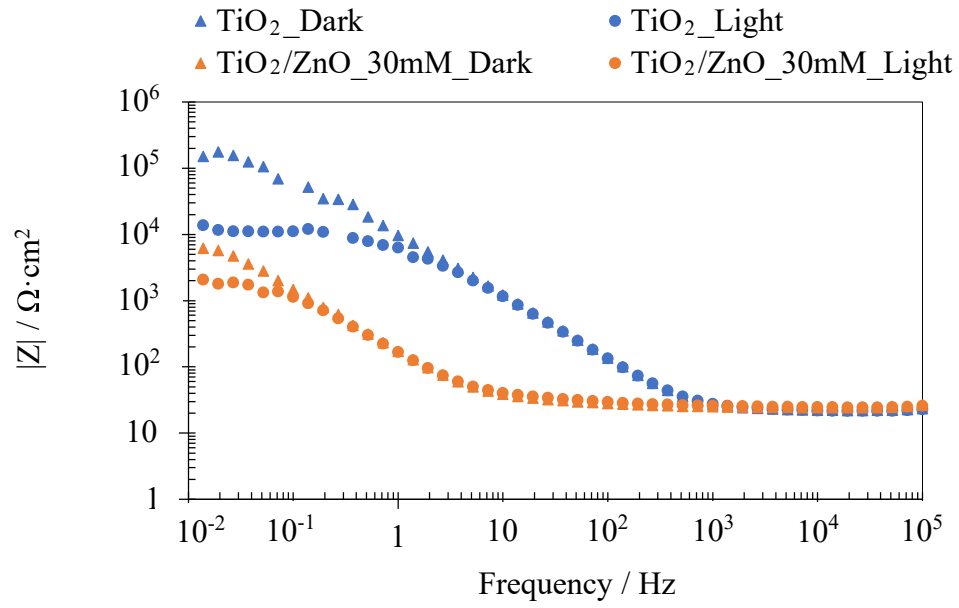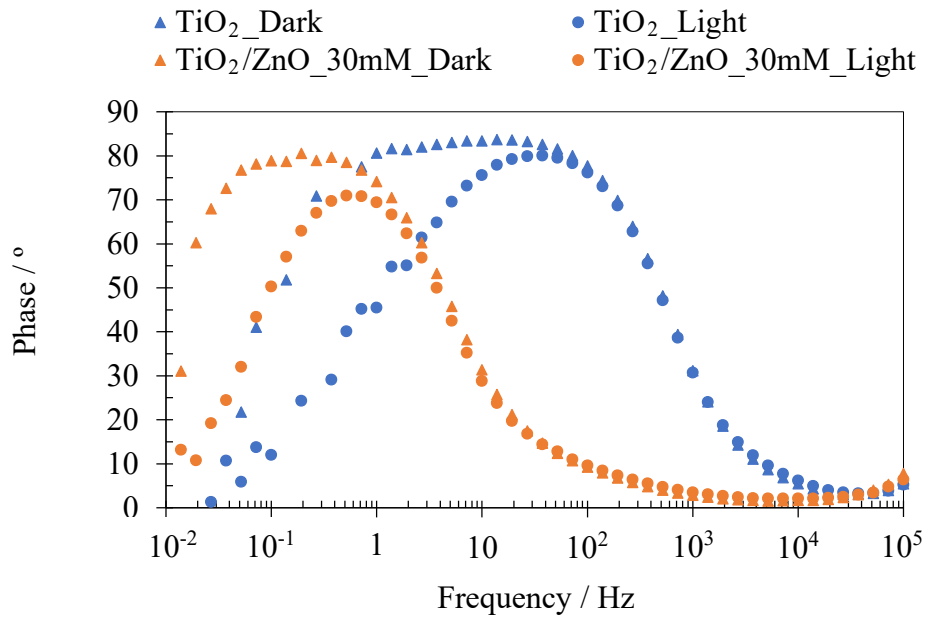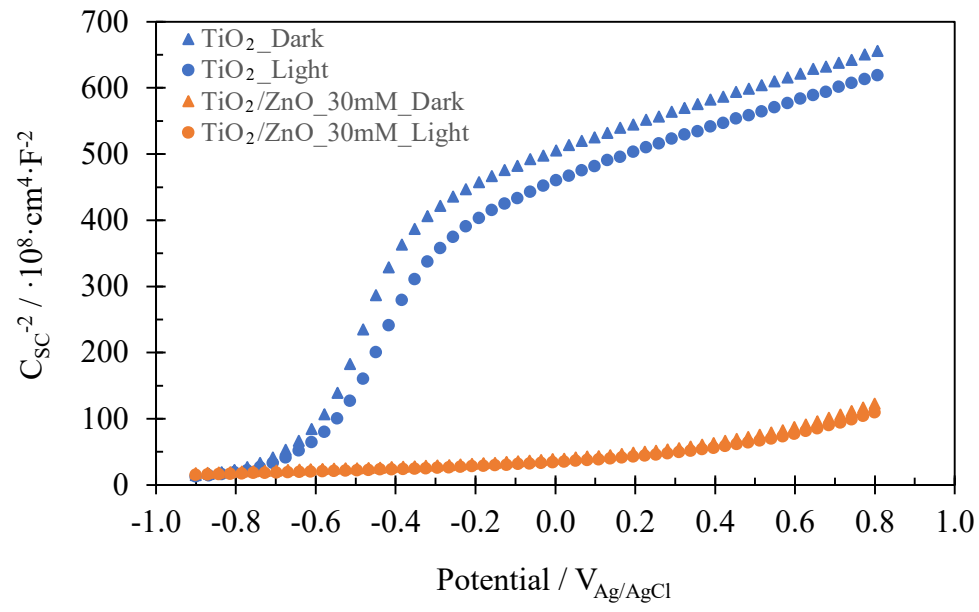
Sample	Ti		O		Zn		O/Ti	O/Zn	Zn/Ti
	Weight ratio	Atomic ratio	Weight ratio	Atomic ratio	Weight ratio	Atomic ratio	Atomic ratio	Atomic ratio	Atomic ratio
TiO_2	63.08	36.33	36.92	63.67	0.00	0.00	1.75	0.00	0.00
TiO_2/Zn_10mM	57.45	34.43	35.44	62.45	7.11	3.12	1.81	20.01	0.09
TiO_2/Zn_20mM	51.62	31.35	34.32	62.40	14.05	6.25	1.99	9.98	0.20
TiO_2/Zn_30mM	44.93	26.99	35.89	64.57	19.18	8.44	2.39	7.65	0.31
TiO_2/Zn_40mM	23.93	16.72	28.09	58.73	47.98	24.56	3.51	2.39	1.47
TiO_2/Zn_50mM	11.34	8.65	24.23	55.34	64.43	36.01	6.40	1.54	4.16
TiO_2/Zn_60mM	5.57	4.31	24.09	55.81	70.34	39.88	12.95	1.40	9.25

Table 2

Sample	Sa (nm)	Sq (nm)
TiO_2	33	40
TiO_2/ZnO_10mM	61	71
TiO_2/ZnO_20mM	61	70
TiO_2/ZnO_30mM	80	91
TiO_2/ZnO_40mM	131	153
TiO_2/ZnO_50mM	125	145
TiO_2/ZnO_60mM	460	530

Table 3

Photocatalyst	Cristallite size (nm)
TiO$_2$/ZnO_10mM	23
TiO$_2$/ZnO_20mM	39
TiO$_2$/ZnO_30mM	44
TiO$_2$/ZnO_40mM	47
TiO$_2$/ZnO_50mM	50
TiO$_2$/ZnO_60mM	58

Table 4

Sample	N_D (x 10^{19} cm^{-3})
TiO$_2$ Dark	0.94
TiO$_2$ Light	1.21
TiO$_2$/ZnO_30mM Dark	10.71
TiO$_2$/ZnO_30mM Light	11.61